Forward modeling of JET polarimetry diagnostic[a)]

Oliver Ford,[1] J. Svensson,[2] A. Boboc,[3] D. C. McDonald,[3] and JET-EFDA Contributors[4,b),c)]
[1]*Blackett Laboratory, Imperial College, London SW7 2BZ, United Kingdom*
[2]*Max Planck Institute for Plasma Physics, Teilinstitut D-17491 Greifswald,Germany*
[3]*Euratom/UKAEA Fusion Association, Culham Science Centre, Abingdon OX14 3DB, United Kingdom*
[4]*JET-EFDA, Culham Science Centre, OX14 3DB Abingdon, United Kingdom*

(Presented 14 May 2008; received 9 May 2008; accepted 18 June 2008; published online 31 October 2008)

An analytical Bayesian inversion of the JET interferometry line integrated densities into density profiles and associated uncertainty information, is demonstrated. These are used, with a detailed model of plasma polarimetry, to predict the rotation and ellipticity for the JET polarimeter. This includes the lateral channels, for over 45,000 time points over 1313 JET pulses. Good agreement with measured values is shown for a number of channels. For the remaining channels, the requirement of a more detailed model of the diagnostic is demonstrated. A commonly used approximation for the Cotton-Mouton effect on the lateral channels is also evaluated. © *2008 American Institute of Physics.* [DOI: 10.1063/1.2956880]

I. INTRODUCTION

The JET interferometry/polarimetry[1] system passes eight linearly polarized far infrared laser beams, four vertically and four laterally through the plasma in the poloidal plane (Fig. 1). For each beam, the change in polarization angle $\Delta\psi$, induced ellipticity ϵ, and the phase variation $\Delta\phi$ is measured. Provided that no rapid changes in density or loss of the signal due to refraction occur during the pulse, causing so-called "fringe jumps," $\Delta\phi$ is routinely and reliably converted to line integrated electron density after subtracting the vibration effects measured by a reference beam.

The rotation $\Delta\psi$ and ellipticity angle $\chi=\tan^{-1}\epsilon$ are commonly related to the electron density n_e and magnetic field $\underline{B}$ by Eqs. (1) (Faraday effect) and (2) (Cotton–Mouton effect). Each of these is strictly only valid when the other effect is small.

$$\Delta\psi \propto \int n_e(z)B_{\parallel}(z)dz \quad \text{for } \chi \approx 0, \tag{1}$$

$$\chi \propto \int n_e(z)B_{\perp}^2(z)dz \quad \text{for } \Delta\psi \approx 0. \tag{2}$$

Here, $\hat{z}$ is the beam direction and for Eq. (2), the polarization angle ψ is 45° to $\underline{B}$ in the (x,y) plane.

The beam perpendicular field $\underline{B}_{\perp}$ is predominantly the toroidal vacuum field which for the vertical channels is approximately constant since it is a strong function of only major radius R. In this case, $\sin\chi$ can be used as a second measure of line integrated density.[2]

For the lateral channels, where $B_{\perp}=f(z)$ (and currently the initial polarization $\psi_0 \neq 45°$), or where either $\Delta\psi$ or χ become large, a complete model for the polarimetry is required.

II. PLASMA POLARIMETRY MODEL

For a complete model of the polarimetry, the polarization is represented as a Stokes vector [Eq. (3)] and its evolution is given by Eq. (4).[3]

$$\underline{s} = (\cos 2\chi \cos 2\psi, \cos 2\chi \sin 2\psi, \sin 2\chi), \tag{3}$$

$$\frac{d\underline{s}}{dz} = \underline{\Omega}(z) \times \underline{s}. \tag{4}$$

For low temperature plasmas ($T_e \lesssim 8$ keV), the vector $\underline{\Omega}(z)$ is given by Eq. (5), known as the cold plasma model. For higher temperatures, where electron cyclotron and relativistic effects must be included, other expressions exist.[4]

$$\underline{\Omega} = \frac{\omega_p^2}{2c\omega^3(1-\omega_c^2/\omega^2)} \begin{bmatrix} (e/m)^2 & (B_x^2 - B_y^2) \\ (e/m)^2 & 2B_xB_y \\ 2\omega(e/m) & B_z \end{bmatrix}, \tag{5}$$

with $\hat{z}$ the beam direction and $\hat{y}$ the toroidal direction. $\psi=0$ when the linearly polarized wave has $\underline{E} \| \hat{y}$.

To evaluate this, Eq. (4) is integrated along each line of sight using $\underline{B}(R,Z)$ provided by the JET equilibrium code EFIT (Ref. 5) and $n_e(R,Z)$ obtained from the interferometry.

III. INTERFEROMETRY

To obtain $n_e(R,Z)$, a Bayesian inversion[6] is performed on the eight measured line integrated densities D_i. The density is modeled as a one dimensional function of normalized poloidal flux Ψ_N. The function used is a linear interpolation of 30 nodes n_{e_j} at regular intervals in $0<\Psi_N<1.2$. For each channel, a forward function/model is assigned. This predicts

[a)]Contributed paper, published as part of the Proceedings of the 17th Topical Conference on High-Temperature Plasma Diagnostics, Albuquerque, New Mexico, May 2008.
[b)]For a full listing of names and affiliations of the JET-EFDA Contributors, see A. T. Macrander, Rev. Sci. Instrum. **79**, 10F701 (2008).
[c)]See the Appendix of M.L.Watkins *et al.*, Fusion Energy 2006 (Proceedings of the 21st International Conference, Chengdu, 2006) IAEA, (2006).

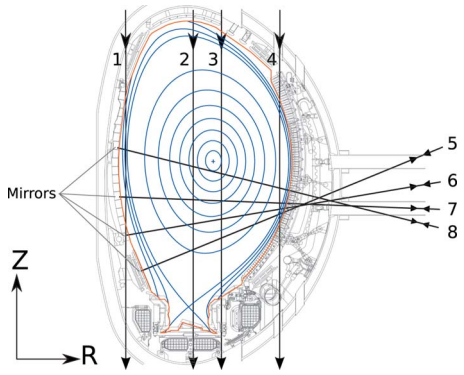

FIG. 1. (Color online) Lines of sight used by the eight JET interferometry and polarimetry channels (numbered), shown with contours of poloidal flux for a typical pulse (blue).

the final data that would be produced, given the physical plasma state, in the absence of random noise and comprises a complete model of both the diagnostic physics and hardware including calibration procedures. In this simple example, the data are taken as the line integrated density and the forward function is simply a linear combination of the density nodes $f_i(\underline{n}_e)=\Sigma_{j=1}^{N} W_{ij} n_{e_j}$, where the weights W_{ij} are determined by the lines of sight for each channel and the flux surface geometry provided by EFIT.

For the likelihood function, which gives the probability distribution of data that could be observed in the presence of random noise, given the plasma state, a Gaussian about $f_i(\underline{n}_e)$ with $\sigma_d=3\times10^{17}$ m^{-2} is used for each channel. Through Bayes theorem, the posterior can be written in terms of this and a prior $P(\underline{n}_e)$ [Eq. (6)].

$$P(\underline{n}_e|\underline{D}) \propto P(\underline{D}|\underline{n}_e)P(\underline{n}_e). \tag{6}$$

The prior used is a single sided independent Gaussian in each node about 0 with $\sigma_p=5\times10^{20}$ m^{-3}. This is primarily to ensure that the inversion is analytical but also well represents the prior knowledge that the density is unlikely to exceed JET's normal operating regime.

The full posterior can be formulated as the truncated multivariate Gaussian in n_e given in Eq. (7), where $\underline{\underline{\sigma}}_D$ and $\underline{\underline{\sigma}}_P$ have only diagonal elements σ_d^2 and σ_p^2.

$$P(\underline{n}_e|\underline{D}) \propto \mathcal{G}(\underline{n}_e;\underline{n}_{e0},\underline{\underline{\sigma}}_{n_e}) \quad \text{for all } n_{e_j} \geqslant 0, \tag{7}$$

with

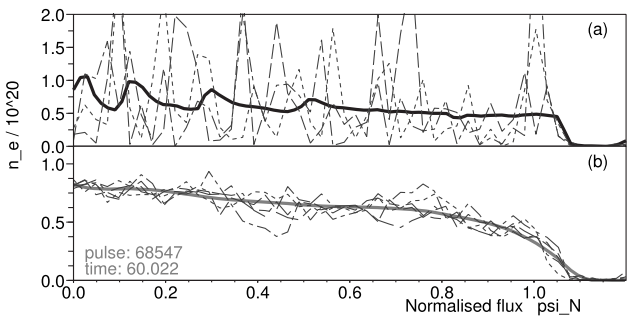

FIG. 2. Maximum posterior (solid) and random samples (broken) of the posterior $P(\underline{n}_e|\underline{D})$ including (a) only weak $n_e<2\times10^{20}$ prior and (b) a strong smoothing prior.

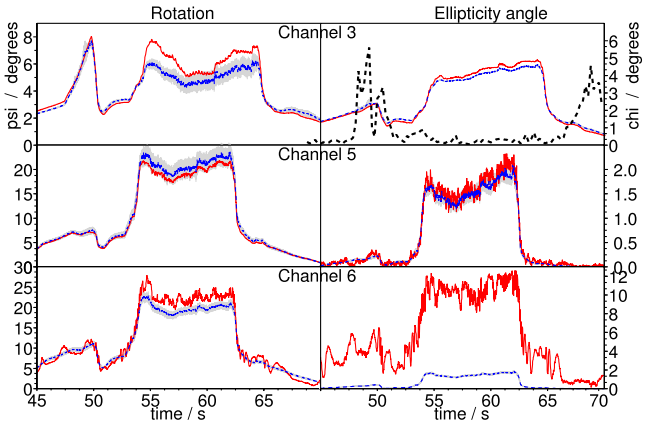

FIG. 3. (Color online) Predicted (blue/dark) vs measured (red/light) ψ (left) and χ (right) for channels 3, 5, and 6. The light gray bands are $\pm2\sigma$ in $P(y|\underline{D},\underline{B})$ so represent the allowable variation within uncertainty of the n_e profile. Also shown for channel 3 (broken line) is the difference (in percent, same scale) between the full model and Eq. (2).

$$\underline{n}_{e0} = \underline{\underline{\sigma}}_{n_e} \underline{\underline{W}}^T \underline{\underline{\sigma}}_D^{-1} \underline{D},$$

$$\underline{\underline{\sigma}}_{n_e} = [\underline{\underline{W}}^T \underline{\underline{\sigma}}_D^{-1} \underline{\underline{W}} + \underline{\underline{\sigma}}_P^{-1}]^{-1}.$$

This gives the probability of any configuration of $\underline{n}_e$ given only $\underline{D}$ and the prior.

Figure 2 shows the highest probability profile and a few random samples using (a) the weak prior described above and (b) a prior favoring similar n_e for neighboring nodes. While the former appears worse, it better represents what is known about the profile from only the line integrated densities.

IV. MODEL EVALUATION

At 500 ms intervals in 1313 pulses, the above inversion was carried out and 300 samples drawn from the posterior. Each sampled profile was used to predict ψ and χ for all eight channels from the model in Sec. II. The mean and standard deviation of these provide a representation of $P(\psi/\chi|\underline{D},\underline{B})$ for that time point.

Figure 3 shows the predicted (ψ_p/χ_p) and measured (ψ_m/χ_m) traces for three channels of a single pulse. Figure 4 shows the predicted points from all the pulses against the measured values.

Despite the large variation in the n_e profiles in Fig. 2(a), the narrow 2σ bands show that the predictions are well

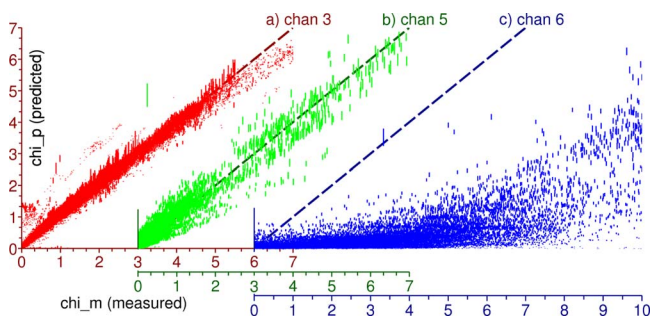

FIG. 4. (Color online) Predicted vs measured (standard processing) ellipticity angle χ for 500 ms samples of 1313 shots for channels (a) 3, (b) 5, and (c) 6. Vertical lengths are $\pm1\sigma$ in allowable variation of n_e.

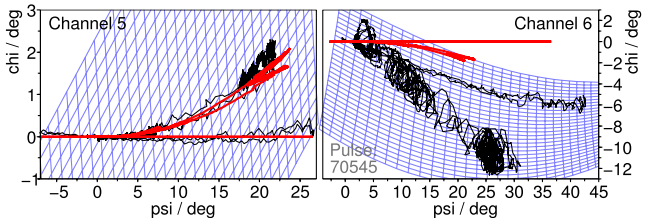

FIG. 5. (Color online) Mapping by Guenther's model of a regular (R,R') grid and measured data (black) to (ψ,χ). Red/light: predicted (ψ_p,χ_p) trace. Both traces also show calibration sweep of ψ with $\chi=0$.

determined from $\underline{D}$ and $\underline{B}$ alone, with χ_p better determined than ψ_p on channel 3. This is expected for the vertical channels which are well approximated by Eq. (2). In this case the difference (broken line) between the approximation and the full calculation is at most 7%, which is much less than the difference between either and the measurement. It is also evident that ψ_p is more sensitive to the exact n_e profile during the high density H-mode phase of this pulse (54–63 s).

Channel 5 shows the best agreement with the measurement and where χ_p is outside the 2σ bands of χ_m, it is likely due to the random fluctuations of χ_m. Neither the systematic nor random uncertainties on ψ_m and χ_m are calculated here. Also not included is the uncertainty in $\underline{B}$ or the flux surface geometry. It is likely that the large disagreement with ψ_m for channel 3 is due to this, since the channel is very sensitive to the plasma core position and field, far from the magnetic sensors on which EFIT is based. Channel 6, which is not normally used due to calibration issues (see Sec. V), shows complete disagreement with the measured χ.

Figure 4 shows the agreement between χ_p and χ_m for the three channels for all 1313 pulses. Again, the best agreement is in channel 5, where no systematic disagreement can be seen. Channel 3 shows good agreement but with a systematically lower prediction at very high χ. Little or no correlation can be seen in channel 6.

V. DIAGNOSTIC MODEL

Each channel has two detectors which measure orthogonal components of a beat signal created by combination of the beam with a 100 kHz modulated beam. The two signals are combined electronically to produce R and R' which ideally relate to ψ and χ by Eqs. (8) and (9),[2] where C, Θ_0, and Φ_0 are determined by a calibration procedure in which ψ_0 is swept through a large range, before the plasma is present.

$$R = C^{-1}\tan(\Theta+\Theta_0)\cos(\Phi+\Phi_0), \tag{8}$$

$$R' = C^{-1}\tan(\Theta+\Theta_0)\sin(\Phi+\Phi_0),$$

$$(\cos 2\Theta, \tan\Phi) = (\cos 2\chi\cos 2\psi, \tan 2\psi/\sin 2\chi). \tag{9}$$

In reality, the $(R,R')\Leftrightarrow(\psi,\chi)$ conversion is not this simple. Guenther[2] proposed an unknown optical component adding an extra phase shift. The extra unknowns are also obtained by the calibration procedure and the model is used to obtain ψ_m and χ_m from (R,R'). In some channels, e.g., 5, this works well but for others, e.g., 6, it does not. Figure 5 shows the $[\psi_m(t),\chi_m(t)]$ trace calculated by Guenther's model as well as a regular (R,R') grid to illustrate the mapping. Also shown is the predicted $[\psi_p(t),\chi_p(t)]$ trace. It is clear from the difference between the trace during the plasma and during the calibration $(\chi=0)$ that the ellipticity information is present, just not correctly extracted. The same issue affects the other channels to varying degrees.

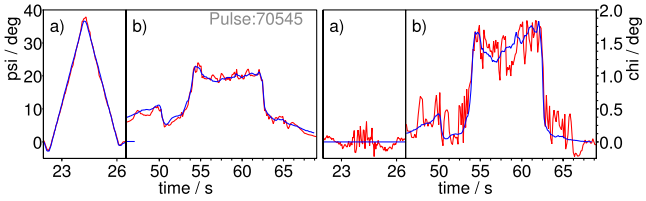

FIG. 6. (Color online) Predicted (blue/dark) and remapped (red/light) ψ and χ during (a) calibration and (b) plasma for channel 6.

Proof of the principle can be demonstrated by finding a mapping which fits (ψ_m,χ_m) to both the predictions (ψ_p,χ_p) and calibration. Figure 6 shows the (ψ_m,χ_m) trace obtained by a fitted linear transformation.

The agreement is well within the random fluctuations. While this does not provide the mapping $(R,R')\Leftrightarrow(\psi,\chi)$, a single transformation fitting the whole pulse and calibration strongly supports the plasma model of Sec. II. Future work will concentrate on developing a model of the diagnostic including calibration, mapping, and mirror vibrations to give the likelihood $P(R,R'|\underline{B},\underline{n_e})$. Combined with other diagnostic likelihoods, such as the interferometry and magnetics,[7] this would give a posterior that provides a consistent picture of the plasma state, including uncertainty information based on all known sources of error.

The use of the full interferometry posterior in predicting the polarimetry measurements, rather than making assumptions about the form of density profile, removes systematic effects that this might introduce. It has been shown how, despite the large apparent variation, these can correctly predict perfectly calibrated channels using the given model. For the less ideal cases, it has been shown that an improved diagnostic model would allow all channels to be used.

ACKNOWLEDGMENTS

This work is being partly funded by an EPSRC CASE studentship with UKAEA Culham and has been carried out within the framework of the European Fusion Development Agreement. The views and opinions expressed herein do not necessarily reflect those of the European Commission.

[1] G. Braithwaite, N. Gottardi, G. Magyar, J. O'Rourke, J. Ryan, and D. Vron, Rev. Sci. Instrum. **60**, 2825 (1989).
[2] K. Guenther, 31st EPS Conference on Plasma Physics, London, 2004 (unpublished), pp. P5–P172.
[3] S. E. Segre, Plasma Phys. Controlled Fusion **14**, R57 (1999).
[4] V. V. Mirnov, W. X. Ding, D. L. Brower, M. Zeeland, and T. N. Carlstrom, Phys. Plasmas **14**, 102105 (2007).
[5] D. P. O'Brien, L. L. Lao, E. Solano, M. Garribba, T. S. Taylor, J. G. Cordey, and J. J. Ellis, Nucl. Fusion **32**, 1351 (1992).
[6] D. Sivia, *Data Analysis: A Bayesian Tutorial* (Oxford University Press, Oxford, 1999).
[7] J. Svensson and A. Werner, "Current Tomography for Axisymmetric Plasmas" Plasma Phys. Controlled Fusion **50**, 085002 (2008).